PHYSICAL REVIEW B **105**, 195137 (2022)

Understanding photoluminescence of Cs_2ZrCl_6 doped with post-transition-metal ions using first-principles calculations

Mingzhe Liu,[1,2] Chang-Kui Duan,[1,2,*] Peter A. Tanner,[3,†] Chong-Geng Ma,[4] Xiantao Wei,[1] and Min Yin[1]
[1]*CAS Key Laboratory of Microscale Magnetic Resonance, and School of Physical Sciences,*
University of Science and Technology of China, Hefei 230026, China
[2]*CAS Center for Excellence in Quantum Information and Quantum Physics,*
University of Science and Technology of China, Hefei 230026, China
[3]*Hong Kong Baptist University, Department of Chemistry, Kowloon, 224 Waterloo Road, Hong Kong, People's Republic of China*
[4]*School of Optoelectronic Engineering & CQUPT-BUL Innovation Institute,*
Chongqing University of Posts and Telecommunications, Chongqing 400065, China

(Received 14 February 2022; revised 22 April 2022; accepted 16 May 2022; published 25 May 2022)

Doped lead-free halide perovskites have been widely reported for impressive photoluminescence properties. Herein we study the mechanisms of photoluminescence in Se^{4+}-, Te^{4+}-, Sb^{3+}-, and Bi^{3+}-doped Cs_2ZrCl_6 and also in this undoped host via first-principles calculations with hybrid density functionals. The results show that the main photoluminescence in the host, as well as isovalent and aliovalent dopants, can be attributed to highly localized self-trapped excitons composed of an electron on Zr and a V_k center (molecular-like Cl_2^-), MCl_6 ($M =$ Se^{4+}, Te^{4+}), and MCl_5 ($M =$ Bi^{3+}, Sb^{3+}) complexes, respectively. The systematic underestimation of the emission energies is discussed and is attributed to the over-relaxation of the excited-state geometric structures. Our results illustrate the photoluminescence processes and excited-state dynamics in host and aliovalent dopant of Cs_2ZrCl_6, which may inspire further revelations of the mechanisms of photoluminescence of other materials in the tetravalent halide perovskite family.

DOI: 10.1103/PhysRevB.105.195137

I. INTRODUCTION

Metal halide perovskites have attracted broad attention in photoluminescent and optoelectronic applications for their remarkable light absorption and photoluminescence quantum yields [1–3]. Our previous systematic first-principles study was mainly focused on revealing the photoluminescent features of trivalent Bi^{3+} and Sb^{3+} ions doped in halide double perovskites and rock-salt-type systems that contain linked MCl_6 octahedra [4]. The so-called "0D" perovskites adopt a spatially isolated MX_6 ($M =$ metal, $X =$ Cl, Br, or I) structure that leads to weak interaction between polyhedra and hence to more localized charge states with the potential to achieve a higher luminescence quantum yield. The cubic host Cs_2ZrCl_6, with a wide band gap and defect tolerance, is among the A_2BX_6 ($A =$ alkali-metal element, $B =$ Sn, Zr, or Hf, $X =$ Cl, Br, or I) series that contain the isolated MX_6 structure, and it has been a focus of various experimental studies exploring its scintillation and photoluminescence properties of the pristine crystal [5,6], the crystal doped with d- or f-element activators [7–18], or the post-transition-metal ions bismuth [19] and antimony [20–23] upon which we focus herein, in addition to tellurium [24–29] and selenium [30]. The Zr^{4+} ions occupy one in every two Cl_6 octahedra alternately and periodically in Cs_2ZrCl_6.

The lone pair ions with the ns^2 configuration, such as Bi^{3+} ($n = 6$), Sb^{3+}, and Te^{4+} ($n = 5$), are frequently used as activators to improve the optical properties of halide perovskites. Their ground states are denoted as $^1S_0$, whereas the sp [short for $(ns)^1(np)^1$] electron configuration splits into four $^{2S+1}L_J$ multiplets, namely $^3P_0$, $^3P_1$, $^3P_2$, and $^1P_1$. Among the excitations to these states, according to the selection rules of electric dipole transitions, the $^1S_0 \rightarrow {}^1P_1$ transition is both orbitally and spin allowed, and the $^1S_0 \rightarrow {}^3P_1$ transition is partially spin allowed via mixing with $^1P_1$ by spin-orbit coupling (SOC), while the $^1S_0 \rightarrow {}^3P_2$ and $^1S_0 \rightarrow {}^3P_0$ transitions are forbidden for the free ion. In hosts, the lowest allowed transition $^1S_0 \leftrightarrow {}^3P_1$ (denoted as the A-band) is usually the most important in photoluminescence. Other transitions, apart from the internal $s^2 \leftrightarrow sp$ transitions, may also play a role. Two types of charge-transfer (CT) transitions involving the host's valence or conduction bands [31,32] and various self-activated luminescence [termed self-trapped exciton (STE) recombination], regardless of whether an intrinsic-defect is present or not, may also be involved. All of those possibilities complicate the interpretation of experimental results and the optimization of performance by structural and compositional design.

In this work, we have carried out first-principles calculations based on density functional theory at the generalized gradient approximation (GGA) level supplemented with calculations with hybrid density functionals. The aims are to explore the most significant defects of the pristine host, and the defects formed by doping post-transition-metal ions, so

---

[*] ckduan@ustc.edu.cn
[†] peter.a.tanner@gmail.com

that the defect levels and their excitation and relaxation processes can be uncovered. This will enable us to provide a systematic understanding of the luminescent phenomena reported experimentally.

II. METHODS

A. Parameter settings

The calculations were carried out with the projector augmented wave method [33] implemented in the Vienna *ab initio* simulation package code [34,35]. The generalized gradient approximation of the Perdew-Burke-Ernzerhof (PBE) functional [36] was employed. The geometric structure relaxation on the unit cell was carried out with 3 × 3 × 3 k-mesh and an energy cutoff of 520 eV. Then the experimental cell parameters were employed to construct the $\sqrt{2} \times \sqrt{2} \times 2$ supercell, and all calculations based on the supercell were carried out under fixed cell parameters and an energy cutoff of 400 eV for the plane-wave expansion. Spin polarization was employed for the host and supercells with intrinsic defects, and SOC was considered for doped supercells, both by employing default magnetic parameter settings. The inclusion of a fraction (denoted as α) of HF exchange significantly widens the bandgap energy and improves the description of excited states of defects and impurities. Here, $\alpha = 0.25$ was adopted as in the standard screened hybrid functional HSE06 [37]. The excited states were achieved by the constrained occupancy method for calculations with SOC and by spin multiplet setting without SOC. The convergence tolerances of energy and residual atomic forces were smaller than 10^{-5} eV and 10^{-2} eV/Å, respectively. The differences of bond lengths between the equilibrium geometric configurations given by 3 × 3 × 3 k-mesh and Γ point are no more than 5×10^{-3} Å. Hence, the Γ-point sampling was adopted as a compromise in structure optimization with the PBE functional and total-energy calculation with HSE06. A mixture of the blocked Davidson iteration scheme and the subsequent residual minimization scheme-direct inversion in the iterative subspace RMM-DIIS algorithm was used for electronic optimization. The band structure was calculated along a high-symmetry k-point path according to Bradley and Cracknell [38] by employing the experimental lattice parameters and 3 × 3 × 3 k-point mesh.

B. Formation energy and charge transition levels of a point defect

The formation energy of a defect X in the charge state of q is defined as [39]

$$E^f[X^q] = E_{\text{tot}}[X^q] - E_{\text{tot}}[\text{bulk}] - \sum_i n_i\mu_i + qE_F, \quad (1)$$

where $E_{\text{tot}}[X^q]$ and $E_{\text{tot}}[\text{bulk}]$ are the (relative) total energies derived from a supercell representing the defect and the pristine host, respectively; n_i is the change in the number of type i atom species, which is added to ($n_i > 0$) or removed from ($n_i < 0$) the perfect supercell; μ_i is the relative chemical potential for type i atom species, and E_F is the electron Fermi energy. *Post hoc* corrections to $E_{\text{tot}}[X^q]$, the total energy of charged defects, were employed, and we followed the method proposed by Durrant *et al.* [40], where the combination of the Lany-Zunger correction [41,42] due to image charge and the potential alignment between neutral systems has been shown to yield accurate corrections for cubic supercells. The detailed procedures have been given by us previously [4] and are not elaborated on here.

The charge transition level (CTL) $X(q_1/q_2)$ for defect X is defined as the Fermi level of the electron reservoir that equilibrates two valence states of energies $E_{\text{tot}}(X^{q_1})$ and $E_{\text{tot}}(X^{q_2})$ of a defect, i.e.,

$$X(q_1/q_2) = \frac{E_{\text{tot}}(X^{q_1}) - E_{\text{tot}}(X^{q_2})}{q_2 - q_1}. \quad (2)$$

When $q_1 = q_2 + 1$, the energy difference of a CTL from the conduction-band minimum (CBM), CBM $- X[q_1/(q_1 - 1)]$, and from the valence-band maximum (VBM), $X[(q_2 + 1)/q_2] -$ VBM, is the energy released when the defect X^{q_1} captures an electron from the CBM and X^{q_2} captures a hole from the VBM, respectively.

III. RESULTS AND DISCUSSION

The tetravalent halide perovskite Cs_2MCl_6 ($M =$ Sn^{4+}, Zr^{4+}, Hf^{4+}) series are isostructural and follow the same pattern in photoluminescence, so that we study Cs_2ZrCl_6 here as the representative of the Cs_2MCl_6 variants. The space group of Cs_2ZrCl_6 is $Fm\bar{3}m$. The lattice constant of the 36-atom cubic unit cell of Cs_2ZrCl_6 obtained with the PBE method modified for solids [43] is 10.382 Å, close to the reported experimental value of 10.428 Å [44], which was employed in all further calculations. The sites and independent coordinates of atoms are listed in Table S1 in the Supplemental Material [45], and they agree with experiment. All the Zr ions show up in tetravalent form with a closed shell in all the supercells and their magnetic moments are zero, except for the case with the electron polaron dominated by the Zr^{3+}-4d orbital component with natural spin polarization.

A. Band-structure properties

The measured optical gap of Cs_2ZrCl_6 is 4.86 eV [47]. The calculation based on the Kohn-Sham (KS) eigenvalues of the PBE calculation [Fig. S2(a) in the Supplemental Material [45] for band structure] produces a substantially underestimated indirect band gap of 3.65 eV, while the energy band calculated with the HSE06 method [Fig. 1(a)] predicts an improved generalized KS band gap of 4.99 eV, which is also indirect. The band structure is similar to the case in the halide double perovskite (elpasolite) family Cs_2NaMCl_6 ($M =$ Sc^{3+}, Y^{3+}, La^{3+}), with the main difference being that the band gap is at least 2 eV narrower. The HSE06 calculation of the density of states (DOS) is plotted in Fig. 1(b). The luminescence of Sb- and Bi-doped Cs_2NaMCl_6 has been attributed to $[SbCl_6]^{3-}$ and $[BiCl_6]^{3-}$ complexes, respectively. The narrower band gap in Cs_2ZrCl_6 may lead to lower CT or metal to metal charge transfer (MMCT) type states rather than $s^2 \rightarrow sp$ excited states, which will be discussed in detail in Sec. III F. It is noted that the band structure in Fig. 1(a) has not taken the SOC into account, as it has no material impact on band structure judging from our calculation with the PBE functional (see

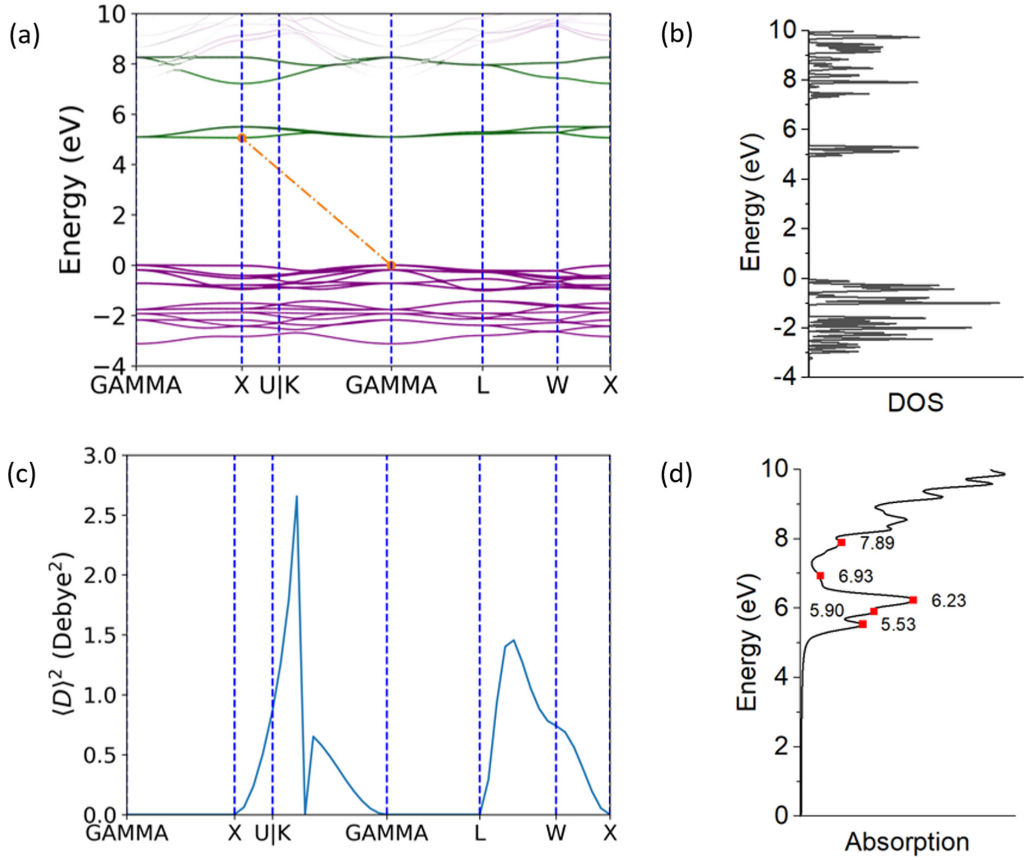

FIG. 1. The band structure (a) and the density of states (b) of Cs_2ZrCl_6 accompanied with (c) the square of the electric dipole transition dipole moment and (d) the absorption spectrum obtained via the calculation of the dielectric tensor. All data are achieved with the HSE06 hybrid density functional. In (a), the bands in purple, dark green, and light purple have Cl-p, Zr-d, and Cs-s/Cl-p as the main components. In (a) and (b), the VBM is set to zero for convenience, and the HSE06 band gap is improved to 4.99 eV from the value of 3.65 eV predicted by the PBE method. In (d), the 6.23 eV absorption peak is close to the value 6.54 eV read off from the measured absorption spectrum reported in [46]. See Fig. S2 in the Supplemental Material [45] for the PBE counterpart of this figure.

Fig. S2 in the Supplemental Material [45] for a comparison of band structures with and without SOC).

The conduction band (CB) and valence band (VB) are mainly of Zr-d and Cl-p character, respectively, which also shape the dominant components of the electron and hole of the pristine STE. The influence of the SOC interaction of Zr on the CB is shown to be negligible in our calculation.

The electric dipole transition is forbidden between the CBM and VBM states, as shown by Fig. 1(c). The absorption spectrum due to the VB to CB transitions is plotted in Fig. 1(d), showing the absorption edge and peaks.

B. Intrinsic defects

Intrinsic defects are important for halide perovskites when considering host photoluminescence. Each isolated single defect is modeled by adding an atom to, removing an atom from, or replacing an atom with another atom in the pristine supercell that contains 32 Cs, 16 Zr, and 96 Cl atoms.

Due to the overbinding of molecules of elements that take on negative oxidation states in solids, the differences in electron localization between the elements in the molecule and the solid can result in substantial errors in DFT calculated formation energies [48]. Therefore, the anion corrections have been adopted to the elementary substances (Cl_2 in this case) according to Ref. [49] in chemical potential calculations.

The allowed chemical potential region, as plotted in Fig. 2(a), is predominantly shaped by CsCl and $ZrCl_4$. In the allowed region, the chemical environment is mainly characterized by the chemical potential of Cl. Therefore, three representative cases in Fig. 2(a) are chosen to find the dominant intrinsic defects in different chemical circumstances, and we denote them as Cl-rich, Cl-moderate, and Cl-poor.

The ionic radii in 6-coordination of Cs^+, Zr^{4+}, and Cl^- are 1.67, 0.72, and 1.81 Å [50], respectively. Antisite defects are subsequently ignored due to the large difference in radius and valence state for these ions. Therefore, we only consider vacancies and interstitials of these ions in the Cs_2ZrCl_6 host.

There is only one type of vacancy for each of Cs, Zr and Cl. However, the situation for interstitial defects is much more complicated. Several candidate sites could accept a $Cl^{0,1-}$ interstitial ion after relaxation, but rather less so for Cs^+ and Zr^{4+}. After comparing the stabilities, two sites have been selected for the discussion of interstitial ions. We denote the vacant center of six Cl^- ions of O_h symmetry as the Cl_6 site, and the site near the center of one Zr^{4+} and two neighboring Cl^- as the Cl_2 site, as shown in Fig. 3. The Cl_6 site can tolerate any of Cs^+, Zr^{4+}, and $Cl^{0,1-}$ ion interstitials, and the

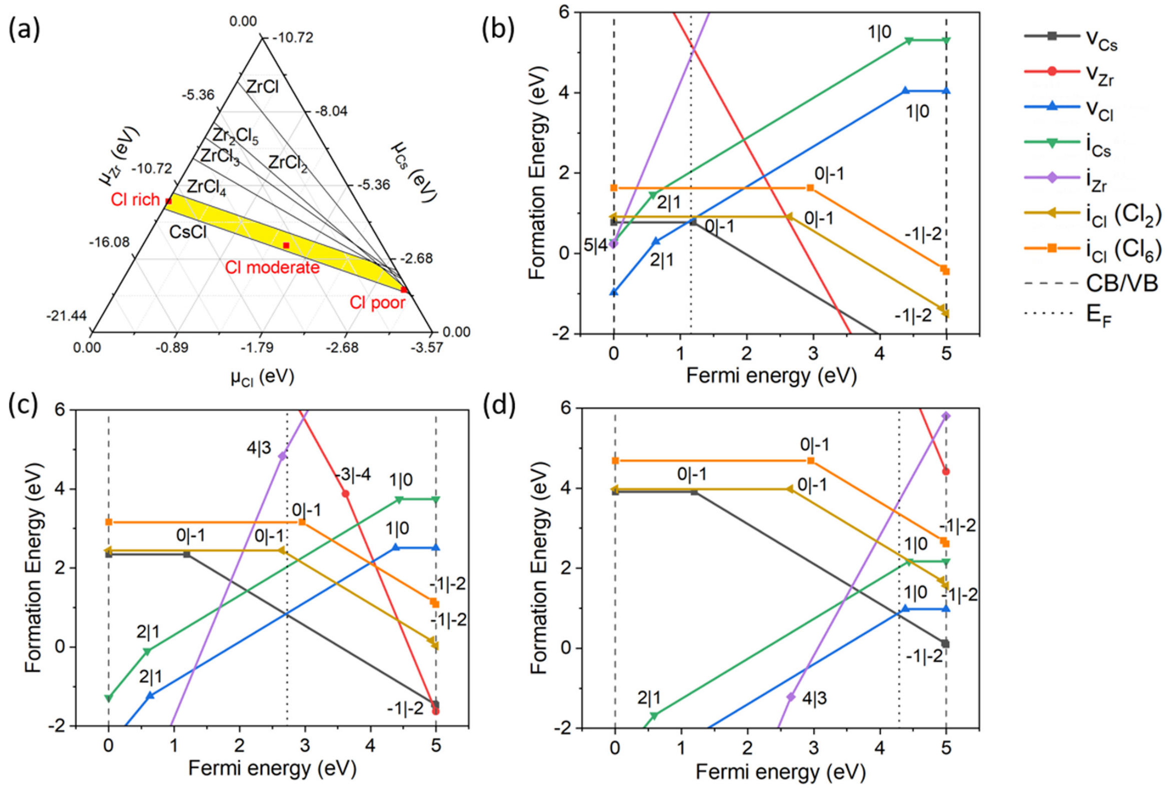

FIG. 2. (a) Allowed ranges of the relative chemical potentials of elements to sustain the Cs_2ZrCl_6 host, and (b)–(d) the formation energies calculated via the PBE method under Cl-rich (b), Cl-moderate (c), and Cl-poor (d) condition as specified in panel (a). The symbols E_F, CB, and VB in the legend represent the Fermi energy determined by charge neutrality and the conduction and valence bands, and the two integers such as "0| − 1" mark the place where the valence of the defect switches from 0 to −1 as the Fermi energy increases. It is noted that the Fermi energy is given relative to VBM via the HSE06 method, and the VBM and CBM obtained by the PBE calculation are at 0.96 and 4.60 eV when the reference potentials of PBE and HSE06 results are aligned.

Cl_2 site only fits the interstitial $Cl^{0,1-}$. Later, in Sec. III C, we study in detail the influence on STE of the $Cl^{0,1-}$ interstitial at the Cl_2 site instead of the one at the Cl_6 site, since the $Cl^{0,1-}$ interstitial at the Cl_2 site is not only energetically more favorable, but it also neighbors the Zr^{4+} site and is more influential on the STE energy than the one at the Cl_6 site.

As shown by the formation energies of intrinsic defects in Fig. 2, among all the intrinsic defects we have considered, vacancies V_{Cs}^{-} and V_{Cl}^{+} charge-balance each other under all significant chemical conditions, whereas the V_{Cs}^{0} and interstitial i_{Cl}^{0} are important only under a Cl-rich condition. V_{Cs}^{0}, V_{Cl}^{0}, i_{Cl}^{0}, i_{Cl}^{-}, and i_{Cs}^{+} are of lower concentration in Cs_2ZrCl_6 but could possibly be common in other tetravalent halide perovskite variants, so they are involved in the discussion in terms of generality. The influence of intrinsic defects to STE in Cs_2ZrCl_6 is discussed in the following section.

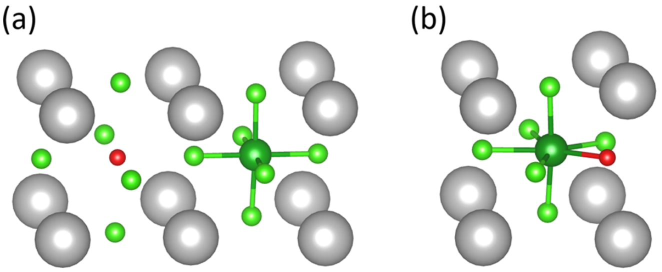

FIG. 3. The two most stable interstitial candidate sites in the Cs_2ZrCl_6 host: (a) the Cl_6 site and (b) the Cl_2 site. The silver, green (large and small), and red spheres in both panels are Cs^+, Zr^{4+}, Cl^- and interstitial sites, respectively.

C. STE-like excitation states

Our calculations show that the STE excited states in the Cs_2ZrCl_6 host can be viewed as an electron on a Zr^{4+} ion and a hole on the surrounding Cl^- ions.

There are two possible STE excited-state configurations, namely the octahedral type with the electron sitting on a center Zr forming Zr^{3+} and the hole distributed on all the surrounding coordinated Cl^- ions, and Zr–Cl_2^- type with Zr^{3+} and two of its six Cl^- ligand ions forming a Cl_2^- by accommodating the hole. The latter cannot be obtained by the GGA-PBE functionals or the meta-GGA functionals such as the SCAN [51] in which the self-interaction of electrons is not well corrected and therefore cannot well describe localized states. The Zr–Cl_2^- type STE calculation requires the structure optimization based on the HSE06 method, which contains a mixing of 0.25 times of the Hartree-Fock exchange interaction. It is more computationally demanding for HSE06 calculation at the $\sqrt{2} \times \sqrt{2} \times 2$ supercell, so the results

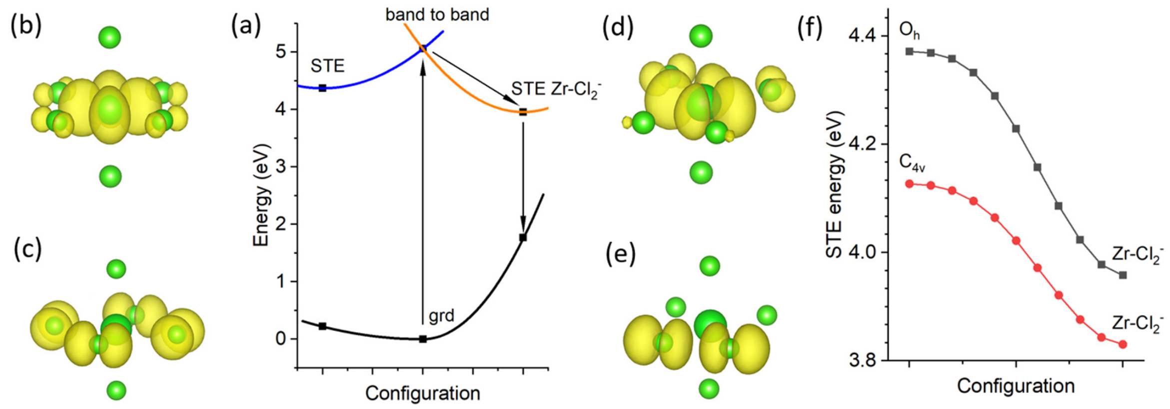

FIG. 4. (a) The configuration coordinate diagram of the STE in the pristine Cs_2ZrCl_6 host. (b),(c) The squared orbital functions of the electron and the hole in the octahedral type STE [left one in (a)]. (d),(e) The same as (b),(c) but in the STE Zr–Cl_2^- that contains a Zr^{3+} (an electron on Zr^{4+}) and a Cl_2^- (V_k center) formed by a hole on two combined Cl^-. (f) The energy curve of STE along the linear interpolation between high-symmetry STE configuration O_h (C_{4v} for the case with a V_{Cl}^+) and the STE Zr–Cl_2^- (the case with a V_{Cl}^+), showing no energy barrier along the considered relaxation routes.

reported hereafter in this subsection are based on the HSE06 method on the conventional cell unless stated otherwise. The octahedral type STE is shown on the left in Fig. 4(a) and has D_{4h} symmetry. The wave functions of the electron and hole of the STE have principal components Zr-d and Cl-p and are plotted in Figs. 4(b) and 4(c), respectively, with the pancake shape. The STE structure is compressed perpendicular to the pancake. The Zr–Cl bonds are 2.47 Å in length for the ground state (no STE), but they increase to 2.50 and 2.55 Å in the axial and equatorial directions, respectively, for the STE state. The Zr–Cl_2^- type STE has a lower symmetry (C_{2v}), and the charge distributions of the electron and hole are shown in Figs. 4(d) and 4(e). The hole in Fig. 4(e) is dominated by Cl-p from two Cl atoms that form a Cl_2^- moleculelike structure that is usually referred to as a V_k center. The distance between the two Cl nuclei in Cl_2^- shrinks from 3.50 Å in the ground-state structure to 2.62 Å, and the Cl_2^- molecule moves away from Zr by 0.1 Å (bond length ~2.64 Å). The more localized hole indicates stronger Coulomb interaction between the electron and hole and larger relaxation, leading to lower energy of the STE state and a larger Stokes shift compared with the octahedral type STE.

As Figs. 4(d) and 4(e) show, the electron and hole are highly localized on Zr and Cl_2^- in $[ZrCl_6]^{2-}$. As a consequence, the emission of the Zr–Cl_2^- type STE is not sensitive to adjacent defects, such as V_{Cs}^-, V_{Cl}^+, and V_{Cs}^0, which would only lead to a weak distortion/limited impact on STE local structure.

Notably, as Fig. 4(f) shows, the Zr–Cl_2^- type STE is about 0.4 eV more stable than the octahedral type, and there is no barrier for the octahedral type STE to relax nonradiatively to the Zr–Cl_2^- type STE. This explains why emission of ~4 eV energy has not been experimentally reported and that the observation of the V_k center has been reported in EPR experiments [5,52].

The excitation and emission energies of STE in the pristine host or with an intrinsic defect are summarized in Table I. Zirconium is tetravalent for V_{Cs}^-, V_{Cl}^+, and i_{Cl}^-, and the Zr–Cl polyhedra take the form of $[ZrCl_6]^{2-}$, $[ZrCl_5]^-$, and $[ZrCl_7]^{3-}$, respectively. In the presence of a V_{Cl}^+ defect, the vertical excitation energy decreases because the symmetry of the complex is lowered from O_h to C_{4v}, resulting in a stronger ligand-field (LF) splitting of the Zr-d state occupied by an electron when the complex is excited. For i_{Cl}^- ($[ZrCl_7]^{3-}$), the addition of an interstitial Cl^- makes the surroundings of Zr more crowded, as shown in Fig. 3(b). The vertical excitation energy is much lower than in the cases of the pristine host and the V_{Cl}^+, as has been indicated by the $(0|-1)$ CTL of i_{Cl}^- in Figs. 2(c) and 2(d).

The Zr ion is still tetravalent for i_{Cl}^0 and V_{Cs}^0, and the Zr–Cl polyhedra take the form of $[ZrCl_7]^{2-}$ and $[ZrCl_6]^{2-}$, respectively. The ground state of i_{Cl}^0 can be viewed as ($[ZrCl_5]^- \cdot Cl_2^-$), and the equilibrium structure of the STE excited state appears as ($[ZrCl_5]^{2-} \cdot Cl_2^0$). The large distortion leads to a large relaxation energy, so the calculated vertical energy difference between the STE and the ground state turns out to be merely 0.29 eV, making i_{Cl}^0 nonluminescent and a quenching center. For V_{Cs}^0, the electron removed together with Cs^+ is taken from two Cl^-, leading to the formation of Cl_2^-, so the ground state can be denoted as ($ZrCl_4^0 \cdot Cl_2^-$). The calculated excited-state equilibrium structure of V_{Cs}^0 can be viewed as ($[ZrCl_2]^+ \cdot 2Cl_2^-$). The excitation and emission energies of V_{Cs}^0 are very similar to those of V_{Cs}^-.

TABLE I. Excitation and emission energy (eV) of STE in the pristine host or with an intrinsic defect.

Type[a]	Pristine	V_{Cs}^-	V_{Cl}^+	i_{Cl}^-	i_{Cl}^0	V_{Cs}^0
Exc	5.06[b]	4.77	4.33	3.37	4.04	4.84
Emi (Sym)	4.15	4.22	3.83	/	/	3.14
Emi (Cl_2^-)	2.21	2.04	2.30	1.62	0.29	1.99
Sym → Cl_2^-	0.41	0.47	0.30			0.84

[a] Exc and Emi stand for vertical excitation and emission, respectively, Sym represents the STE with the same symmetry as the ground state, and Sym → Cl_2^- denotes the energy of relaxation from "Sym" to Cl_2^-.

[b] Revised to 4.74 eV by the HSE06 method on the $\sqrt{2} \times \sqrt{2} \times 2$ supercell optimized with the PBE functional.

The defect V_{Cl}^{0} (i.e., $[\mathrm{ZrCl}_5]^{2-}$ complex) is the only one considered that has an additional electron on a defect level near the CB. The trion STE state [53] of the ZrCl_5^{2-} complex with two electron polarons near the CB and a hole polaron near the VB can relax stepwise to a series of other lower excited states, and it does not contribute to luminescence.

Combining the energies of the STE in the presence of intrinsic defects and the relative importance of these defects in terms of concentration, the STE luminescence can be attributed to be the pristine host, possibly subject to the influence of V_{Cs}^{-}, V_{Cl}^{+}, and V_{Cs}^{0}. Their excitation energies agree reasonably well with the experimentally reported excitation band at 4.8 eV recorded by monitoring the 2.7 eV emission band of the host [19,20]. We attribute the underestimation of the emission energy, also encountered frequently below, to the over-relaxation in the Zr–Cl_2^{-} type STE state in our calculations.

D. Main defects after doping and their levels in the band gap

Here we consider the dopants Se^{4+}, Te^{4+}, Sb^{3+}, and Bi^{3+}. All these free ions have a filled s^2 orbital in their ground state, and their excited states are of the *sp* configuration, which is oriented instead of being spherically symmetric as in the ground state. When different ions with a similar s^2 lone pair are doped in the same host, they behave differently due to their different ionic radius, SOC, and electron-phonon coupling, apart from the inherent difference in electron configuration. These ions are divided into groups: tetravalent Se and Te, which are isovalent to Zr^{4+}, and trivalent Sb and Bi, which are aliovalent to Zr^{4+}.

For the negatively charged aliovalent doping, the most important charge compensator is V_{Cl}^{+}. Here we consider the two extreme cases, one with an adjacent Cl vacancy (V_{Cl}^{+}) and the other with a remote V_{Cl}^{+} whose impact can be totally ignored. The two cases are denoted as $[M\mathrm{Cl}_5]^{2-}$ and $[M\mathrm{Cl}_6]^{3-}$, respectively. The other dominant intrinsic defect, V_{Cs}^{-}, should be away from the negatively charged aliovalent doping centers due to Coulomb repulsion. Hence, we calculate the case $[\mathrm{SeCl}_6]^{2-}$ with a V_{Cs}^{-} nearby to characterize the influence of V_{Cs}^{-} upon the photoluminescence of an s^2 lone pair.

The dopants and compounded defects are also modeled with the $\sqrt{2} \times \sqrt{2} \times 2$ supercell, and the effective concentration is much higher than those in an actual experiment. Fortunately, the impact on the excitation and emission energies would be small, as the interaction between dopants is weak due to the localization of the electronic states (as shown in Figs. 7(b) and 7(c) and Figs. 9(b) and 9(c), and Figs. S6–S8 of the Supplemental Material [45]).

The calculated formation energy line segments of Se and Te dopants together with those of the intrinsic defects can be applied along with the given chemical condition of synthesis and the charge-neutrality condition to determine the dominant defects, just like the cases in Figs. 2(b)–2(d) for intrinsic defects. For the case of $\mathrm{Cs}_2\mathrm{ZrCl}_6$ doped with Se or Te, the dominant dopant-related defect is always $\mathrm{Se}_{\mathrm{Zr}}$ (i.e., Se^{4+}) or $\mathrm{Te}_{\mathrm{Zr}}$ (i.e., Te^{4+}), although the saturation concentration is much lower for Se than Te. The case of doping Sb in $\mathrm{Cs}_2\mathrm{ZrCl}_6$ under Cl-moderate condition is plotted in Fig. 5, which shows that the dominant Sb-related defect is $(\mathrm{Sb}_{\mathrm{Zr}} + V_{\mathrm{Cl}})^0$ (i.e., the $[\mathrm{SbCl}_5]^{2-}$ complex). The situation is similar for doping Sb under a Cl-poor condition and doping Bi under Cl-moderate or -poor conditions, while for the Cl-rich case, the dominant effect for doping Sb is the decrease of the Fermi energy E_F in Fig. 5 [see Fig. S5(b) for details]. Then $\mathrm{Sb}_{\mathrm{Zr}}^{+}$ and $\mathrm{Bi}_{\mathrm{Zr}}^{0}$ (with less $\mathrm{Bi}_{\mathrm{Zr}}^{-}$ and $\mathrm{Bi}_{\mathrm{Zr}}^{+}$) dominate in concentration over the compounded defects $\mathrm{Sb}_{\mathrm{Zr}} + V_{\mathrm{Cl}}$ and $\mathrm{Bi}_{\mathrm{Zr}} + V_{\mathrm{Cl}}$ as the chemical potential increases, respectively. The defects Sb^{5+}, Bi^{4+}, and Bi^{5+} can be excited by ligand to metal CT transitions, but they will not emit but relax to the ground states nonradiatively as a result of large structure relaxation.

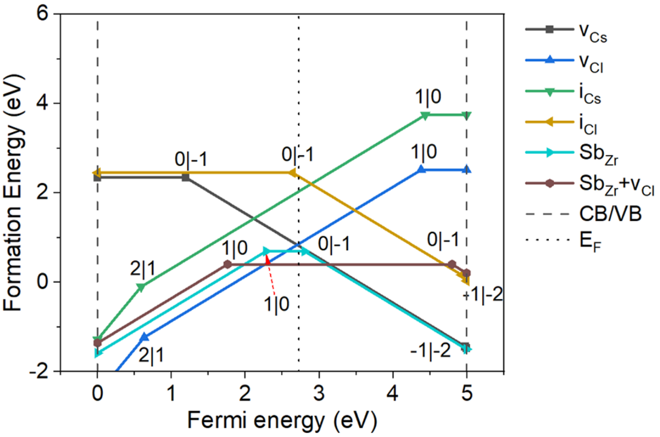

FIG. 5. Formation energy line segments for defects involving Sb doping under a Cl-moderate circumstance. The upper bound of the chemical potential Sb under this condition is determined by the coexistence of $\mathrm{Cs}_3\mathrm{Sb}_2\mathrm{Cl}_9$, and the appropriate value is adopted. Refer to Fig. 2 for other notation.

To illustrate the electronic structure of the doped systems, the diagram of CTLs is plotted in Fig. 6.

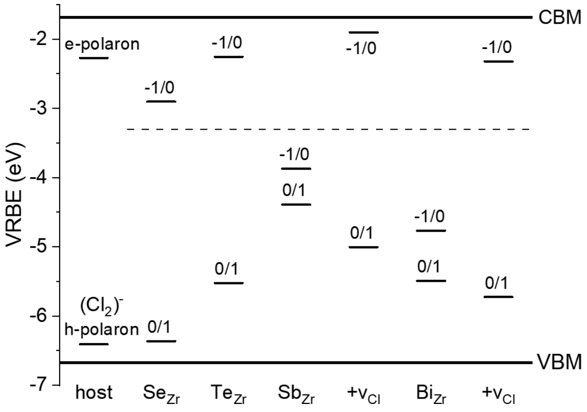

FIG. 6. Vacuum referred bind energies of CTLs and polaron levels in the band gap calculated with the HSE06 method. Note: the e-polaron is an extra electron localized on the Zr^{4+} ion, and the h-polaron is a hole on two adjacent Cl^{-} ions forming Cl_2^{-} after relaxation. The $+\mathrm{v}_{\mathrm{Cl}}$ to the right of $(\mathrm{Sb/Bi})_{\mathrm{Zr}}$ is the compounded defect $[(\mathrm{Sb/Bi})_{\mathrm{Zr}} + V_{\mathrm{Cl}}]$. The electronic configurations for the CTLs of defects (excluding the polarons) above the dashed line are $(ns)^2np/(ns)^2$ and those underneath are $(ns)^2/(ns)$, except that (0/1) of $(\mathrm{Sb/Bi})_{\mathrm{Zr}}$ is $(ns)^1/(ns)^0$.

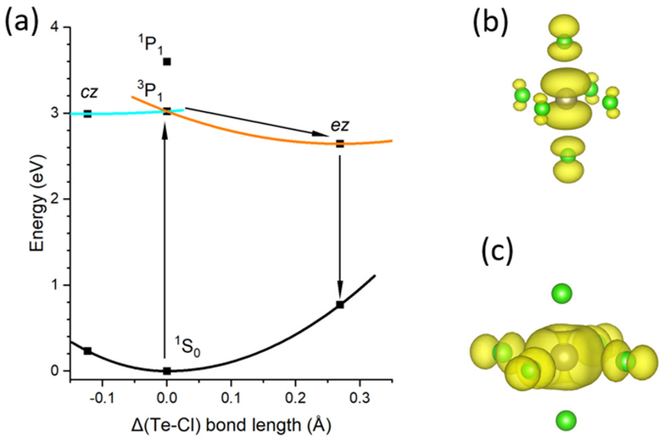

FIG. 7. The configuration coordinate diagram of $\mathrm{Te}^0_{\mathrm{Zr}}$ (Te^{4+}) in $\mathrm{Cs_2ZrCl_6}$ (a) and the squared orbital functions of the excited state at configurations *ez* (b) and *cz* (c), which represent elongated and compressed TeCl_6^{2-} octahedra, respectively. Δ(Te-Cl) in panel (a) is the difference of bond length of the axial (Te-Cl) bond from the average.

The CTLs can be applied to derive the zero-phonon line (ZPL) energies of the CT transitions that involve the total energies (zero-point) of two different geometric configurations. The latter are different from the energies for vertical excitation and emission transitions, which are calculated at the ground and excited equilibrium geometric configurations, respectively. For the $M(s^2)$ dopant involved here, the ZPL energy of the $M(s^2) \to [M(s^1) + e_{\mathrm{CBM}}]$ MMCT transition is $\mathrm{cb_{ZPL}} = \mathrm{CBM} - M(s^2/s^1)$, and the ZPL energy of the $M(s^2) \to [M(s^2p) + h_{\mathrm{VBM}}]$ (ligand to metal) CT transition is $\mathrm{vb_{ZPL}} = M(s^2p/s^2) - \mathrm{VBM}$.

In the $\mathrm{Cs_2ZrCl_6}$ crystal, $M\mathrm{Cl_6}$ ($M =$ Se^{4+}, Te^{4+}, Sb^{3+}, and Bi^{3+}) polyhedra have O_h site symmetry in the ground state, but only D_{4h} site symmetry or even lower in the *sp* excited states; the $M\mathrm{Cl_5}$ ($M =$ Sb^{3+} and Bi^{3+}) polyhedron has C_{4v} site symmetry in both the ground state and the *sp* excited state.

The SOC interaction is a vital factor in discussing the splitting of the *p* states in O_h symmetry and the local structure of $M\mathrm{Cl_6}$ ($M =$ Te^{4+} or Bi^{3+}) in the *sp* states, and it has a noticeable impact on the energies of transition involving excited states for $M =$ Sb^{3+}. Under O_h symmetry, the SOC interaction determines the splitting of *sp* excited states. When SOC is strong enough to compete with the effect of electron-phonon coupling that causes the LF splitting of *np* states, there are two local minima on the excited-state adiabatic potential energy surface (APES), as shown in Fig. 7. The vertical transition from the lower one of the two should be readily observed in luminescence, but observation of the other transition depends on the stability of its population.

E. Photoluminescence of Se and Te dopants

Here we focus on isovalent substitution systems. The CTLs in Fig. 6 indicate that $\mathrm{Se}^0_{\mathrm{Zr}}$ and $\mathrm{Te}^0_{\mathrm{Zr}}$ have both hole trap $[(ns)^2/(ns)]$ and electron trap $[(ns)^2np/(ns)^2]$ defect levels in the band gap. Hence, the lowest excitation band and the emission band should be $s^2 \leftrightarrow sp$ transitions, with the ZPL energy similar to or slightly smaller than the gap between the two CTLs by following the observation for $M^{3+} = \mathrm{Sb}^{3+}$, Bi^{3+} of $(M\mathrm{Cl_6})^{3-}$ in a variety of halides [4].

Similar to the case of trivalent ions in $(M\mathrm{Cl_6})^{3-}$ octahedra [4], a twofold stretching mode ε_g dominates the distortion in the geometric configuration of *sp* excited states of the activator ion, and there are two local equilibria (or one being a saddle point with SOC turned off) denoted as *ez* and *cz*, characterized by the two axial ligands being longer or short than those of the other equatorial four.

Taking Te^{4+}-doped $\mathrm{Cs_2ZrCl_6}$ as an example, there are two local minima in the excited-state potential surface of the $^3P_1$ state corresponding to *ez* and *cz* configurations as the configuration coordinate diagram shows in Fig. 7. We simplify for convenience by calling the lowest *sp* excited state $^3P_1$ even after the structure relaxation, although for the limiting case of large structure relaxation, the state manifests the $2S + 1 = 3$ spin multiplet components of the *sp* states, composed of *ns* orbit coupling with the lowest crystal-field orbital of *np*. For the $\mathrm{Cs_2ZrCl_6}$:Te^{4+} system, the *ez* geometric configuration is of lower energy and exhibits a larger Stokes shift than for *cz*. A 580 nm emission has been reported experimentally [24–26], which is attributed to the emission of the *ez* configuration. The Se^{4+} ion has a similar electron configuration to that of Te^{4+}, but of smaller ion radius and a weaker SOC. Therefore, the structure relaxation of the *sp* states and the splitting of *np* should be dominated by electron-phonon coupling and LF interaction as a consequence of lower symmetry, respectively. Such differences between Se and Te are responsible for the smaller $^1P_1$–$^3P_1$ energy difference of 0.25 eV for Se than 0.58 eV for Te, and the larger Stokes shift of 1.99 eV for Se compared with 1.15 eV for Te, as listed in Table II. As for $[\mathrm{SeCl_6}]^{2-}$ with a nearest V_{Cs}^-, its excitation is quite close to the case without V_{Cs}^-, and its emission decreases by merely 0.19 eV (1.46–1.27 eV). The local structure of $[\mathrm{SeCl_6}]^{2-}$ with V_{Cs}^- is plotted in Fig. S1 in the Supplemental Material [45].

The results in Table II were obtained by optimizing the structure via the HSE06 method for the conventional cell, except that the data in parentheses were obtained by the HSE06 method on $\sqrt{2} \times \sqrt{2} \times 2$ supercell structures optimized successfully with the PBE functional. Differences between the two methods are an indication of the lower limit of the uncertainties in the calculated results. The calculation can reasonably well describe the experimental data for the excitation bands of Se- and Te-doped $\mathrm{Cs_2ZrCl_6}$, while the emission energies are underestimated again.

F. Photoluminescence of Sb,Bi complexes

Considering $[\mathrm{SbCl_6}]^{3-}$ and $[\mathrm{ZrCl_6}]^{2-}$, it is inferred from Fig. 6 that the MMCT state of $[\mathrm{SbCl_6}]^{3-}$ (i.e., the hole sitting on $[\mathrm{SbCl_6}]^{3-}$ but the electron localizing on $[\mathrm{ZrCl_6}]^{2-}$) is more favorable in energy than $s^2 \to sp$ and STE excited states. However, the $[\mathrm{SbCl_6}]^{3-}$ and $[\mathrm{ZrCl_6}]^{2-}$ octahedra are separated spatially in the “0D” perovskite $\mathrm{Cs_2ZrCl_6}$, and such an MMCT state is expected to be substantially or even fully quenched [4].

Furthermore, we have calculated the energy curves of the lowest *sp* excited state and the MMCT state along grd-*sp*, grd-MMCT, and *sp*-MMCT with SOC, and the results are plotted

TABLE II. The calculated and measured excitation and emission energies (in units of eV) of Se^{4+}, Te^{4+}, and two sets of Sb^{3+}- and Bi^{3+}-related defects in Cs_2ZrCl_6.

	Calculated				Measured	
Defect	$^3P_{1,0}$	$^1P_1$	*ez*	*cz*	exc	emi
Se_{Zr}	3.19 (3.30)	3.46 (3.55)	1.46 (1.31)	2.53[b]	3.23 [30]	1.77 [30]
$Se_{Zr} + V_{Cs}^{-}$[a]	3.16		1.27			
Te_{Zr}	3.16 (3.02)	3.75 (3.60)	2.00 (1.87)	2.76[b]	3.18 [26], 3.10 [25]	2.16 [24–26]
Sb_{Zr}^{-}	3.55 (3.20)	4.03 (3.71)	2.27	2.73[b]	3.94 [20,23]	2.53 [20,22,23]
$Sb_{Zr}^{-} + V_{Cl}^{+}$	3.44 (3.22)	4.31 (4.16)	1.67 (1.60)		3.81, 4.35 [22]	2.07 [20,22,23]
Bi_{Zr}^{-}	3.64 (3.43)	5.26 (5.04)	3.36 (3.26)	3.47		
$Bi_{Zr}^{-} + V_{Cl}^{+}$	3.36 (3.20)	4.82 (4.65)	2.31 (2.46)		3.49 [19]	2.72 [19]

[a] Calculated to test the impact of nearest V_{Cs}^{-}.

[b] Saddle point in the potential surface.

in Fig. 8. The figure shows that after being excited to the *sp* states by a vertical transition from the ground state, the excited $[SbCl_6]^{3-}$ complex will quickly relax to the equilibrium geometric configuration of the $^3P_1$ state, as shown by the *sp*-grd segment in Fig. 8. There is a possible nonradiative relaxation route: at room temperature, the 0.30 eV energy barrier cannot thoroughly hinder its relaxation by thermal activation to the MMCT state of 0.57 eV lower in energy, and then it will relax nonradiatively to the ground state. The higher-energy $^1P_1$ excited state would have more of a tendency to relax to the MMCT state than $^3P_1$ does. We note that the relaxation of the MMCT state to the Zr–Cl_2^- type STE is hindered, as the CTL of Sb^{3+}/Sb^{4+} lies higher than the hole polaron in Fig. 6, which prevents the hole on Sb from relaxing to the Cl's in the $[ZrCl_6^{2-}]$ complex.

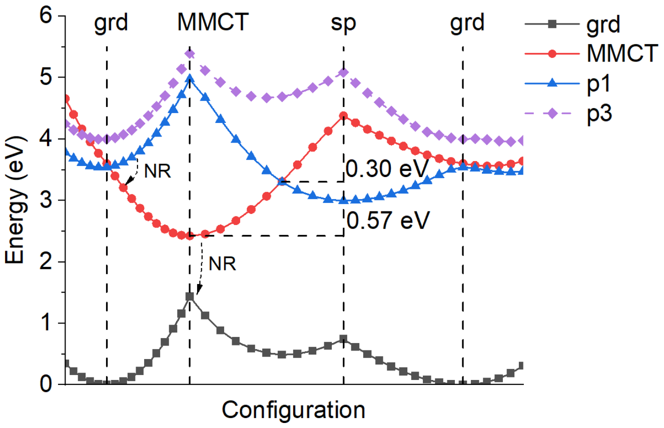

FIG. 8. The configuration coordinate diagram of $Cs_2ZrCl_6:Sb^{3+}$ along three linearly interpolated routes grd–MMCT, MMCT–sp, and sp–grd. Here the structures "grd," "MMCT," and "sp" represent the equilibrium geometric configuration of the ground state, $(Sb_{Zr} + Zr_{Zr}^{-})$, and the $^3P_1$ excited state, respectively. The curves "grd," "MMCT," and "p1" and "p3" plot the energies of the ground state, MMCT, and the $^3P_1$ and $^1P_1$ states, respectively. NR is short for nonradiative relaxation and denotes two important relaxation processes. It is noted that under (near) highly symmetric structures "grd" and "MMCT," the $^1P_1$ and $^3P_1$ are the states of Sb^{3+} with one electron excited from Sb-*s* to $j = 1/2$ (the lowest two) and $j = 3/2$ (the other four) Sb-*p* orbitals split dominantly by SOC. Under other distorted structures, the *sp* electronic configuration splits to many more states due to the combination of SOC, ligand-field, and Coulomb interactions. Here the energies of the $^1P_1$ and $^3P_1$ states are estimated by the single electron excitations from Sb-*s* to the lowest and the third Sb-*p* throughout.

As for Bi, there are two pathways for nonradiative relaxation, whose barriers are only 0.19 and 0.18 eV (see Fig. S4 in the Supplemental Material [45]), smaller than that in the case of Sb. This explains no observed emission for the $[BiCl_6]^{3-}$ defect (Table II).

Figure 5 shows that $[SbCl_5]^{2-}$ $([Sb_{Zr}^{-} + V_{Cl}^{+}]^0)$ is more favorable in formation energy than $[SbCl_6]^{3-}$ $([Sb_{Zr}^{-})$ under the Cl-moderate condition, and it even remains so under the Cl-poor condition.

The $[SbCl_5]^{2-}$ complex has a point group symmetry of C_{4v} and is subject to strong electron-phonon coupling or LF interaction. The configuration coordinate diagram of $[SbCl_5]^{2-}$ is plotted in Fig. 9(a). Just as for $[SeCl_6]^{2-}$, the strong electron-phonon coupling induces a large structure relaxation, i.e., a large Stokes shift. The 5*p* and 5*s* orbitals calculated at the relaxed excited-state structure are plotted in Figs. 9(b) and 9(c), showing the 5*p* orbital along the axial direction and the stretch of 5*s* orbital into an oval due to the impact of the missing Cl^-. With regard to $[BiCl_5]^{2-}$, although the SOC of Bi is much stronger than that of Sb, their *sp* state structures show the same pattern (as shown in Table III) in that the single axial Cl^- ion opposite to the Cl vacancy moves slightly closer to the center ion in the ground state, but markedly away from the center in the *sp*-type excited states.

TABLE III. The bond lengths in $[SbCl_5]^{2-}$ and $[BiCl_5]^{2-}$ complexes for equilibrium ground-state (grd) and *sp* excited-state (exc) geometrical configurations (in units of Å).

Dopant	Bond (counts)	grd	exc
Sb	Axial Cl (×1)	2.45	2.90
	Equatorial Cl (×4)	2.61	2.53
Bi	Axial Cl (×1)	2.53	2.92
	Equatorial Cl (×4)	2.68	2.66

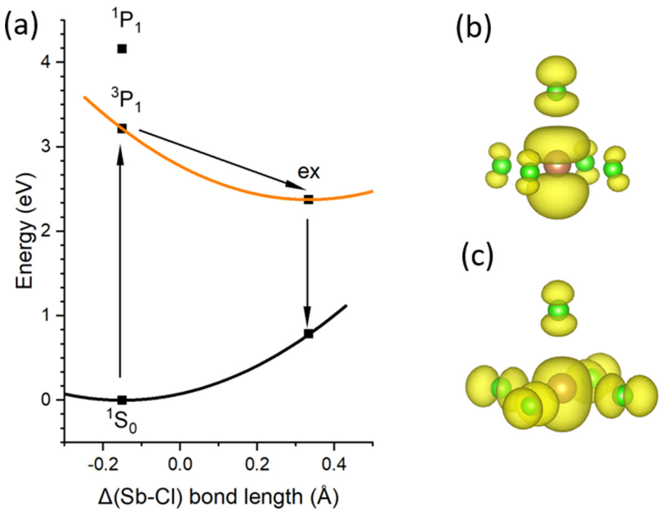

FIG. 9. (a) The configuration coordinate diagram of $[SbCl_5]^{2-}$ complex in Cs_2ZrCl_6, and (b),(c) the square of the orbital functions nominally named Sb-5*p* and Sb-5*s* in the relaxed electronic excited states. Δ(Sb-Cl) in panel (a) means the bond length difference of the C_4 axial (Sb-Cl) bond with respect to the average of the five bonds. The system at $^3P_1$ or $^1P_1$ state will relax nonradiatively to the luminescent state to emit a photon.

TABLE IV. The calculated lattice deformation energy (E_{rlx}), the phonon frequency ($\hbar\omega$) for the model dominating the structure relaxation, and the Huang-Rhys factor (S) of the considered complexes in the Cs_2ZrCl_6 host.

Complex	E_{rlx} (eV)	$\hbar\omega$ (meV)[a]	S[b]
$SbCl_6^{3-}$	0.723	24.6	29.4
$SbCl_5^{2-}$	0.902	29.0	31.1
$BiCl_6^{3-}$ *cz*	0.099	26.7	3.70
$BiCl_6^{3-}$ *ez*	0.273		10.2
$BiCl_5^{2-}$	0.481	29.6	16.3
$SeCl_6^{2-}$	0.797	27.7	28.8
$TeCl_6^{2-}$ *cz*	0.234	28.7	8.13
$TeCl_6^{2-}$ *ez*	0.575		20.0

[a] The phonon frequency $\hbar\omega$ involved in the deformation of dopants in Cs_2ZrCl_6 has been reported experimentally in Cs_2ZrCl_6:Se as 29.8 meV by analyzing the vibrational fine structure [30]; in Cs_2ZrCl_6:Te as 29.8 meV by analyzing the vibrational fine structure [24,25] and as 34.7 meV by fitting the temperature-dependent FWHM curve [26]; and in Cs_2ZrCl_6:Bi as 29.6 meV by fitting the temperature-dependent FWHM curve [56].

[b] The Huang-Rhys factors have been reported as 14.1 [26] and 16.24 [56] for Te and Bi, respectively.

The calculated $s^2 \leftrightarrow sp$ excitation and emission energies of both $[(Sb/Bi)Cl_6]^{3-}$ [i.e., $(Sb/Bi)_{Zr}^-$] and $[(Sb/Bi)Cl_5]^{2-}$ [i.e., $(Sb/Bi)_{Zr} + V_{Cl}$] are listed in Table II, together with the experimental band maxima [19,20].

We attribute the emission of Cs_2ZrCl_6:Bi to the $[BiCl_5]^{2-}$ complex and the dominant lower-energy emission of Cs_2ZrCl_6:Sb to the $[SbCl_5]^{2-}$ complex, as the large formation energy makes the $(Sb/Bi)_{Zr}^-$ octahedral complex less important in terms of concentration, and the excited $(Sb/Bi)_{Zr}^-$ relaxes nonradiatively to the MMCT excited state and subsequently to the ground state. The data in Table II show that the emission energies of $[SbCl_5]^{2-}$ and $[BiCl_5]^{2-}$ complexes are underestimated relative to those reported experimentally by 0.40 eV (1.67 versus 2.07 eV) and 0.41 eV (2.31 versus 2.72 eV), respectively. We envisage that the underestimation is related to the over-relaxation of the excited-state structure via the density functional calculations in use, since a small overestimation of the extent of the large relaxation will lead to a substantial overestimation of relaxation energy and an underestimation of the emission energy. Actually, a recent benchmark of various density functionals on $MAPbI_3$ [54] (MA = methylammonium) has shown, apart from various errors in energies, the overestimation of cell volume by the PBE method, the improvement by including van der Waals interactions, and the potential improvement via certain meta-GGA methods, which we are not going to detail here. To test our suspicion, we have performed the same calculation on an organic system $(C_9NH_{20})_2SbCl_5$, where neat isolated $[SbCl_5]^{2-}$ complexes produce strong red emission [55], and we obtained a similar underestimation of the emission by 0.3 eV. We have also calculated the phonon spectrum of pristine and doped Cs_2ZrCl_6 and obtained the vibration that dominates the structure relaxation of the excited state from the ground-state geometry configuration. Furthermore, we obtained the Huang-Rhys factor by dividing the relaxation energy by the obtained phonon frequency (energy). The results are listed in Table IV, and they support our assignment of the photoluminescence mechanisms.

To sum up, the reported 2.53 and 2.07 eV emissions [20,22,23] in Sb-doped Cs_2ZrCl_6 are attributed to the $^3P_1 \rightarrow {}^1S_0$ emissions of $[SbCl_6]^{3-}$ and $[SbCl_5]^{2-}$ complexes, respectively. The reported 4.35 and 3.81 eV excitation peaks [22] by monitoring the 600 nm emission are attributed correspondingly to $^1S_0 \rightarrow {}^1P_1$ and $^1S_0 \rightarrow {}^3P_1$ transitions of $[SbCl_5]^{2-}$, and the 3.94 eV excitation peak [20,23] is attributed to the $^1S_0 \rightarrow {}^3P_1$ transition of $[SbCl_6]^{3-}$. It is noted that no observed excitation can be attributed for certain to $^1S_0 \rightarrow {}^1P_1$ in $[SbCl_6]^{3-}$. This is not unexpected, as the ionization of the excitation to the conduction band would be much faster for the high-lying $^1P_1$ than $^3P_1$ states. For Bi doping, the reported 3.49 eV excitation and 2.72 eV emission in Bi-doped Cs_2ZrCl_6 [19] is attributed to the $^3P_1 \rightarrow {}^1S_0$ transition of the $[BiCl_5]^{2-}$ complex, while no emission is expected for $[BiCl_6]^{3-}$ due to the faster ionization of the excitation to the MMCT state.

IV. CONCLUSIONS

The band structure, intrinsic defect, and related self-trapped excitons, and the defects introduced by Se, Te, Sb, and Bi doping, including their stabilities and photoluminescent properties, have been thoroughly studied via first-principles calculations based on the PBE density functional supplemented by the HSE06 plus SOC method. The results show that the intrinsic defects V_{Cs}^- and V_{Cl}^+ are dominant and balance with each other in the Cs_2ZrCl_6 host regardless of the chemical potential conditions; a highly localized STE denoted as Zr–Cl_2^- contributes to the luminescence in the host, which could tolerate V_{Cs}^-, V_{Cl}^+, and V_{Cs}^0. The doping of Se or Te leads to isovalent defects $\mathrm{Se}_{\mathrm{Zr}}$ or $\mathrm{Te}_{\mathrm{Zr}}$, respectively. They have similar properties to the isovalent Sb doped in $\mathrm{Cs_2Na(La/Y)Cl_6}$ reported previously [4], which produces $sp \rightarrow s^2$ emission. The most common forms of defects for Sb and Bi doping are $\mathrm{Sb}_{\mathrm{Zr}}^{-} + V_{\mathrm{Cl}}^{+}$ ($[\mathrm{SbCl_5}]^{2-}$) and $\mathrm{Bi}_{\mathrm{Zr}}^{-} + V_{\mathrm{Cl}}^{+}$ ($[\mathrm{BiCl_5}]^{2-}$), leading to red and blue emission, while those $\mathrm{Sb}_{\mathrm{Zr}}^{-}$ (i.e., the $[\mathrm{SbCl_6}]^{3-}$ complex) and $\mathrm{Bi}_{\mathrm{Zr}}^{-}$ (i.e., the $[\mathrm{BiCl_6}]^{3-}$ complex) with remote charge compensation are less important in concentration. Furthermore, the excited $[\mathrm{SbCl_6}]^{3-}$ complex can partially relax to the MMCT state and then to the ground state by thermal activation, explaining the observed weak cyan emission, while the excited $[\mathrm{BiCl_6}]^{3-}$ complex is quenched more thoroughly. The calculation can well describe the excitation band of Se-, Te-, Sb-, or Bi-doped $\mathrm{Cs_2ZrCl_6}$, but it underestimates the energies of the emission bands. The latter failure is attributed to the over-relaxed excited-state structure, similar to the case of $\mathrm{(C_9NH_{20})_2SbCl_5}$, where neat isolated $[\mathrm{SbCl_5}]^{2-}$ complexes produce strong red emission. Our results illustrate the photoluminescence processes and excited-state dynamics in the $\mathrm{Cs_2ZrCl_6}$ host and in post-transition-metal-doped $\mathrm{Cs_2ZrCl_6}$, which may inspire further revelations of the mechanisms and the optimization of photoluminescent properties of materials in the tetravalent halide perovskite family.

ACKNOWLEDGMENTS

The numerical calculations were performed on the supercomputing system at the Supercomputing Center of the University of Science and Technology of China. M.L. and C.-K.D. acknowledge the financial support of the National Key Research and Development Program of China (Grant No. 2018YFA0306600) and Anhui Initiative in Quantum Information Technologies (Grant No. AHY050000). X.W. and M.Y. acknowledge the financial support of the National Natural Science Foundation of China (Grant No. 11974338). C.-G.M. gratefully acknowledges the support from the National Natural Science Foundation of China (Grant No. 52161135110) and the China-Poland Intergovernmental Science and Technology Cooperation Program (Grant No. 2020[15]/10). In our work, the formation energies of compounds when determining chemical potentials of elements are from Materials Project [57]. We have also used VASPKIT [58] and VESTA [59] to display our results.

---

[1] D. Shi, V. Adinolfi, R. Comin, M. Yuan, E. Alarousu, A. Buin, Y. Chen, S. Hoogland, A. Rothenberger, K. Katsiev, Y. Losovyj, X. Zhang, P. A. Dowben, O. F. Mohammed, E. H. Sargent, and O. M. Bakr, Science **347**, 519 (2015).

[2] H. Cho, S.-H. Jeong, M.-H. Park, Y.-H. Kim, C. Wolf, C.-L. Lee, J. H. Heo, A. Sadhanala, N. Myoung, S. Yoo, S. H. Im, R. H. Friend, and T.-W. Lee, Science **350**, 1222 (2015).

[3] Q. A. Akkerman, G. Rain, M. V. Kovalenko, and L. Manna, Nat. Mater. **17**, 394 (2018).

[4] M. Liu, C.-K. Duan, P. A. Tanner, C.-G. Ma, and M. Yin, J. Phys. Chem. C **125**, 26670 (2021).

[5] M. Buryi, V. Babin, R. A. M. Ligthart, S. S. Nagorny, V. B. Mikhailik, V. e. Vaněček, L. Prouzová Prochazková, R. Kandel, V. V. Nahorna, and P. Wang, J. Mater. Chem. C **9**, 2955 (2021).

[6] K. Saeki, Y. Fujimoto, M. Koshimizu, T. Yanagida, and K. Asai, Appl. Phys. Express **9**, 042602 (2016).

[7] Z. Barandiaran and L. Seijo, J. Chem. Phys. **119**, 3785 (2003).

[8] M. Wermuth and H. Gudel, J. Am. Chem. Soc. **121**, 10102 (1999).

[9] P. A. Tanner, J. Dexpert-Ghys, Z. W. Pei, and J. Lin, Chem. Phys. **215**, 125 (1997).

[10] A. G. Page, S. V. Godbole, and M. D. Sastry, J. Lumin. **51**, 335 (1992).

[11] D. Piehler, W. K. Kot, and N. Edelstein, J. Chem. Phys. **94**, 942 (1991).

[12] D. Strand, R. Linder, and H. Schemidtke, Mol. Phys. **71**, 1075 (1990).

[13] P. A. Tanner, Spectrochim. Acta, Part A **46**, 1259 (1990).

[14] C. D. Flint and P. A. Tanner, Mol. Phys. **61**, 389 (1987).

[15] C. D. Flint and P. A. Tanner, Mol. Phys. **53**, 429 (1984).

[16] C. D. Flint and P. A. Tanner, Mol. Phys. **53**, 437 (1984).

[17] C. D. Flint and P. A. Tanner, Mol. Phys. **53**, 801 (1984).

[18] A. R. Reinberg and S. G. Parker, Phys. Rev. B **1**, 2085 (1970).

[19] G. Xiong, L. Yuan, Y. Jin, H. Wu, Z. Li, B. Qu, G. Ju, L. Chen, S. Yang, and Y. Hu, Adv. Opt. Mater. **8**, 2000779 (2020).

[20] B. Chen, Y. Guo, Y. Wang, Z. Liu, Q. Wei, S. Wang, A. L. Rogach, G. Xing, P. Shi, and F. Wang, J. Am. Chem. Soc. **143**, 17599 (2021).

[21] J. Zhou, X. Yun, R. Wang, D. Xu, and X. Li, Mater. Chem. Front. **5**, 6133 (2021).

[22] R. Liu, W. Zhang, G. Li, and W. Liu, Inorg. Chem. Front. **8**, 4035 (2021).

[23] C. Chen, J. Xiang, Y. Chen, M. Jin, J. Zheng, N. Zhang, and C. Guo, Ceram. Int. **48**, 1851 (2022).

[24] H. Donker, W. Smit, and G. Blasse, J. Phys. Chem. Solids **50**, 603 (1989).

[25] P. J. H. Drummen, H. Donker, W. M. A. Smit, and G. Blasse, Chem. Phys. Lett. **144**, 460 (1988).

[26] T. Chang, Q. Wei, R. Zeng, S. Cao, J. Zhao, and B. Zou, J. Phys. Chem. Lett. **12**, 1829 (2021).

[27] Z. Li, Z. Rao, Q. Li, L. Zhou, X. Zhao, and X. Gong, Adv. Opt. Mater. **9**, 2100804 (2021).

[28] Y. Liu, Y. Wu, Z. Juan, X. Sun, W. Zhang, H. Zeng, and X. Li, Adv. Opt. Mater. **9**, 2100815 (2021).

[29] S. Nagorny, Physics **3**, 320 (2021).

[30] H. Donker, W. Van Schaik, W. Smit, and G. Blasse, Chem. Phys. Lett. **158**, 509 (1989).

[31] B. Lou, J. Wen, J. Cai, Y.-Y. Yeung, M. Yin, and C.-K. Duan, Phys. Rev. B **103**, 075109 (2021).

[32] Z. Feng, B. Lou, M. Yin, Y.-Y. Yeung, H.-T. Sun, and C.-K. Duan, Inorg. Chem. **60**, 4434 (2021).

[33] P. E. Blöchl, Phys. Rev. B **50**, 17953 (1994).

[34] G. Kresse and J. Hafner, Phys. Rev. B **47**, 558 (1993).

[35] G. Kresse and J. Hafner, Phys. Rev. B **49**, 14251 (1994).

[36] J. P. Perdew, K. Burke, and M. Ernzerhof, Phys. Rev. Lett. **77**, 3865 (1996).

[37] J. Heyd, G. E. Scuseria, and M. Ernzerhof, J. Chem. Phys. **118**, 8207 (2003).

[38] H. Wondratschek, Acta Crystallogr., Sect. A **29**, 581 (1973).

[39] C. Freysoldt, B. Grabowski, T. Hickel, J. Neugebauer, G. Kresse, A. Janotti, and C. G. Van de Walle, Rev. Mod. Phys. **86**, 253 (2014).

[40] T. R. Durrant, S. T. Murphy, M. B. Watkins, and A. L. Shluger, J. Chem. Phys. **149**, 024103 (2018).

[41] S. Lany and A. Zunger, Phys. Rev. B **78**, 235104 (2008).

[42] S. Lany and A. Zunger, Modell. Simul. Mater. Sci. Eng. **17**, 084002 (2009).

[43] J. P. Perdew, A. Ruzsinszky, G. I. Csonka, O. A. Vydrov, G. E. Scuseria, L. A. Constantin, X. Zhou, and K. Burke, Phys. Rev. Lett. **100**, 136406 (2008).

[44] G. Engel, Z. Kristallogr.-Cryst. Mater. **90**, 341 (1935).

[45] See Supplemental Material at http://link.aps.org/supplemental/10.1103/PhysRevB.105.195137 for details of the information of pristine and doped Cs_2ZrCl_6 structures; the PBE results of band structure, density of states, square of electric dipole transition dipole moment, and absorption spectrum; the spin-orbit coupling impact of band structure and energy bands; the barrier between the *sp* state and the MMCT state for $[BiCl_6]^{3-}$; the formation energies of intrinsic and doped defects under various chemical environments; and the square wave function of Cs_2ZrCl_6 STE with intrinsic defects

[46] P. Cheng, D. Zheng, L. Feng, Y. Liu, J. Liu, J. Li, Y. Yang, G. Wang, and K. Han, J. Energy Chem. **65**, 600 (2022).

[47] S. Liu, B. Yang, J. Chen, D. Wei, D. Zheng, Q. Kong, W. Deng, and K. Han, Angew. Chem., Int. Ed. **59**, 21925 (2020).

[48] D. C. Patton, D. V. Porezag, and M. R. Pederson, Phys. Rev. B **55**, 7454 (1997).

[49] A. Wang, R. Kingsbury, M. McDermott, M. Horton, A. Jain, S. P. Ong, S. Dwaraknath, and K. A. Persson, Sci. Rep. **11**, 15496 (2021).

[50] R. D. Shannon, Acta Crystallogr., Sect. A **32**, 751 (1976).

[51] J. Sun, A. Ruzsinszky, and J. P. Perdew, Phys. Rev. Lett. **115**, 036402 (2015).

[52] R. Král, V. Babin, E. Mihóková, M. Buryi, V. V. Laguta, K. Nitsch, and M. Nikl, J. Phys. Chem. C **121**, 12375 (2017).

[53] R. Ahumada-Lazo, J. A. Alanis, P. Parkinson, D. J. Binks, S. J. O. Hardman, J. T. Griffiths, F. Wisnivesky Rocca Rivarola, C. J. Humphrey, C. Ducati, and N. J. L. K. Davis, J. Phys. Chem. C **123**, 2651 (2019).

[54] H. Xue, G. Brocks, and S. Tao, Phys. Rev. Materials **5**, 125408 (2021).

[55] C. Zhou, H. Lin, Y. Tian, Z. Yuan, R. Clark, B. Chen, L. J. van de Burgt, J. C. Wang, Y. Zhou, K. Hanson, Q. J. Meisner, J. Neu, T. Besara, T. Siegrist, E. Lambers, P. Djurovich, and B. Ma, Chem. Sci. **9**, 586 (2018).

[56] C. Wang, Y. Li, Q. Lv, H. Zheng, G. Zhu, X. Xu, and Y. Wang, Chem. Eng. J. **431**, 134135 (2022).

[57] A. Jain, S. P. Ong, G. Hautier, W. Chen, W. D. Richards, S. Dacek, S. Cholia, D. Gunter, D. Skinner, G. Ceder, and K. a. Persson, APL Mater. **1**, 011002 (2013).

[58] V. Wang, N. Xu, J.-C. Liu, G. Tang, and W.-T. Geng, Comput. Phys. Commun. **267**, 108033 (2021).

[59] K. Momma and F. Izumi, J. Appl. Crystallogr. **44**, 1272 (2011).